Supplementary Information

Measurement-Model Closure of Sub-20 nm Particle Charge Fractions under Varying Trace Gas Composition

Fabian Schmidt-Ott[1,2], Robert Nishida[3,4], Sebastian Schmitt[5], Jason Olfert[6], George Biskos[2,7], Juha Kangasluoma[1]

[1] Institute for Atmospheric and Earth System Research, University of Helsinki, 00014, Helsinki, Finland
[2] Climate & Atmosphere Research Centre, The Cyprus Institute, 2121 Nicosia, Cyprus
[3] Department of Mechanical & Mechatronics Engineering, University of Waterloo, Waterloo, Ontario, Canada
[4] Atmose Ltd, Edmonton, Alberta, Canada
[5] Institute for Occupational Safety and Health (IFA), German Social Accident Insurance (DGUV), 53757 Sankt Augustin, Germany
[6] Department of Mechanical Engineering, University of Alberta, Edmonton, Alberta, Canada
[7] Faculty of Civil Engineering & Geosciences, Delft University of Technology, Delft, The Netherlands

Section S-1. Biases in model output arising from averaging ion properties

A challenge in predicting particle charge distributions with charging models is that the measured ion properties are widely distributed rather than represented by a single value. In practice, the measured Z_i-distribution is often reduced to the concentration-weighted mean mobility $\langle Z_i \rangle$. $\langle m_i \rangle$ is either computed from $\langle Z_i \rangle$ or directly measured. From these mean ion properties, the mean combination coefficient $\langle \beta \rangle$ is then calculated (Eq. 5 in the main text). However, because β depends nonlinearly on Z_i and m_i, and the ion properties are typically widely distributed, using the weighted averages of Z_i and m_i to compute everything else inevitably introduces a bias in $\langle \beta \rangle$, i.e., $\langle \beta(Z_i, m_i) \rangle \neq \beta(\langle Z_i, m_i \rangle)$.

This averaging bias is strongly reduced if ion properties are narrowly distributed, which can for example be reached when introducing VMS to the carrier gas, as shown in the manuscript.

Interestingly, in the sub-20 nm regime, which is close to the ion free molecular limit ($r_\mathrm{p} \ll \lambda_\mathrm{i}$), the combination coefficient is linearly proportional to the ion mean thermal speed (White, 1951):

$$\beta_{a \ll \lambda} = \pi {r_\mathrm{p}}^2 \bar{c}_i \cdot \varepsilon^{-\frac{e^2}{r_\mathrm{p} k_\mathrm{B} T}} \quad , \qquad \text{Eq. S-1}$$

which can potentially reduce this averaging error significantly.

However, typically ion mass is used as main model input (besides electrical mobility) from which $\bar{c}_i$ is determined. Given that m_i and $\bar{c}_i$ are not linearly proportional and therefore $\langle \bar{c}_i(m_i) \rangle \neq \bar{c}_i(\langle m_i \rangle)$ when averaging wide distributions, a similar averaging error is introduced when using $\langle m_i \rangle$ as model input.

For all the model calculations shown in the manuscript, it was therefore important to determine the measured weighted mean of $\bar{c}_i$ as accurately as possible. This was done by converting the measured Z_i-distribution into a $\bar{c}_i$-distribution using the mass-mobility relationship by (Mäkelä et al., 1996) and gas kinetic theory, from which $\langle \bar{c}_i \rangle$ was determined (Eq. 12 in the main text).

Section S-2. Long desorption times of impurities in tubing

Figure S-1 shows the ion masses, evolving over time as silicone conductive tubing was installed at $T = 0$ h and subsequently removed to leave the system flush out. Here, ion mass was computed from the ion electrical mobility using the Kilpatrick (1971) mass–mobility relationship refined by Mäkelä et al. (1996) to aid chemical identification of the species. D2 to D6 correspond to the VMS molecules $(Si(CH_3)_2O)_2$ to $(Si(CH_3)_2O)_6$, appearing as peaks at regularly spaced intervals in the figure, in some cases with an attached NH_4 adduct (Keller et al., 2008).

The figure shows that it can take around 3-12 hours until the mobility distribution of positive ions returns to be approximately constant over time. This indicates that impurities introduced into the system gradually desorb from the inner tubing walls. For measurements of charger ions and repeatable particle charging, it is therefore important to flush the system for sufficiently long periods before measuring electrical mobility. The figure also indicates that even after 12 hours, smaller VMS molecules appear to remain present in the system, likely originating from O-rings. On the other hand, the mobility distribution of the negative ions does not significantly change over time.

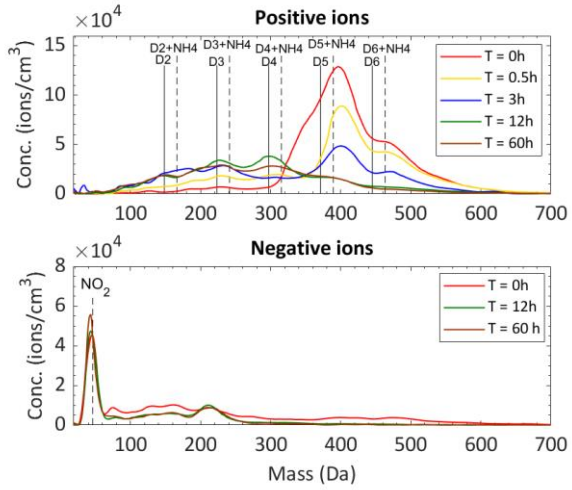

Figure S-1. Ion mass distributions at various time points following removal of the conductive silicone tubing upstream of the ionizer at T=0h.

Section S-3. Verification of steady-state conditions

The development of the steady-state charge was compared for a variety of configurations summarized in Table S-1.

Table S-1. Configurations of the charge conditioners used. The flow distributor consists of a flat plate positioned opposite the charger's inlet and has the function to suppress jet formation and redistribute the flow across the charger's cross section. This increases the residence time of the aerosol inside the charger and thereby increases the *nt*-product.

	Source	Activity	Dimensions (cm)	Volume (cm^3)	Flow Distributor	Arrangement
Config. 1	^{63}Ni	370 MBq	10×3×1.5 (rectangle)	45	No	single
Config. 2	^{241}Am	185 MBq	7×5.6 (cylinder, L×d)	172	No	single
Config. 3 *	^{63}Ni	370 MBq	10×3×1.5 (rectangle)	45 (×2)	No	two in-series
Config. 4	^{241}Am	50 MBq	10×5.7 (cylinder, L×d)	255.2	Yes	single

*used for all measurements shown in the manuscript

Particles entering the charge conditioner(s) were either positively or negatively charged depending on the voltage applied across the upstream DMA 1. This makes it possible to accurately determine whether a steady-state charge distribution has been reached, because a charge distribution at steady-state is identical regardless of whether positively or negatively charged particles enter the charge conditioner.

Figure **S-2** shows the measured positive and negative charge fractions using all configurations shown in Table S-1, where particles entering the charge conditioner were either positively charged, indicated by a "+" and "-" symbol, respectively. It shows that when using configs. 1 and 2, a charge equilibrium was not reached: when positively charged particles were passed through the neutralizer, a significant fraction of particles retained their initial positive charge after passing through the charger. Similarly, when initially negatively charged particles were passed through the charger, most particles remained negatively charged.

On the other hand, steady-state conditions were reached for both configs. 3 and 4, i.e., using two ^{63}Ni chargers in-series or using an ^{241}Am charger with a flow-disturbing plate. In both cases, neutralization was complete, as particles with initially positive and negative charges showed identical charge distributions.

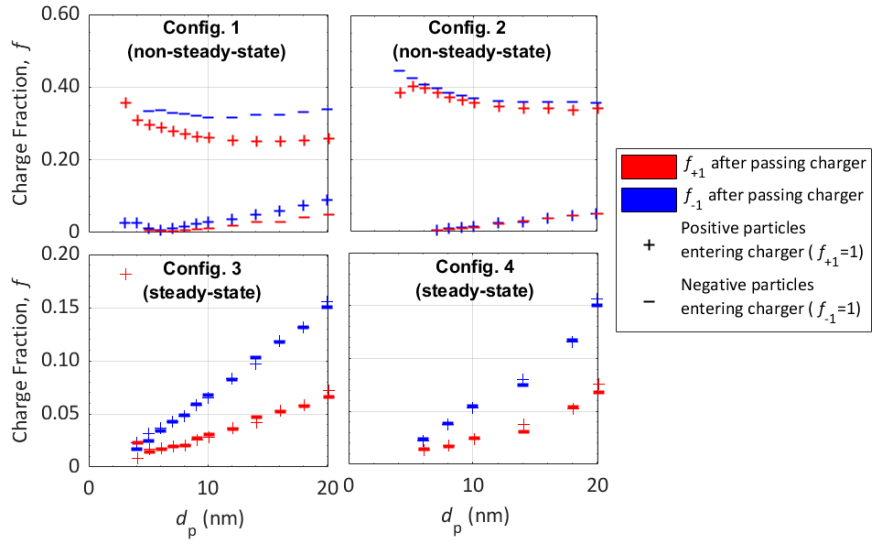

Figure S-2. Charge fractions produced by a ^{63}Ni and ^{241}Am charger, where particles are initially negatively charged.

Given that steady-state equilibrium was achieved when using a flow-conditioning plate (config. 4), whereas steady state was not achieved when the flow-conditioning plate was omitted (config. 2), suggests that a jet forms inside the charger, reducing particle residence time and thereby preventing the establishment of steady-state equilibrium.

Furthermore, the residence time when using a single ^{63}Ni charger (config. 1) shows to be insufficient to achieve a steady-state charge distribution, whereas it is sufficient when operating two ^{63}Ni chargers in series (config. 3). These findings demonstrate that adequate interaction time between charger ions and particles is critical for achieving steady-state equilibrium and, consequently, reproducible particle charge fractions.

The results indicate that steady-state charging conditions for sub-20 nm particles are often not attained when using conventional charge neutralizers available in laboratories. Under non-steady-state conditions, particle charging remains limited by ion-particle interaction, causing the resulting charge distributions to depend on charger-specific parameters, i.e., the ion concentration (n) and particle residence time (t). As a result, different neutralizers can yield significantly different charge distributions if the nt product is too low. Different radioactive chargers produce similar charge distributions only when the bipolar steady-state distribution is reached. The steady-state particle charge fractions are then governed primarily by the properties of the charging ions, as we have shown in the paper.

Section S-4. Electrostatic Precipitator

Figure S-3 shows a schematic of the custom-made ESP, which consisted of a stainless-steel tube placed between two Tee-unions (Swagelok, Ohio, USA), through which a voltage rod (stainless steel) passed that was held in place and electrically insulated by a two Teflon ferrules at each end.

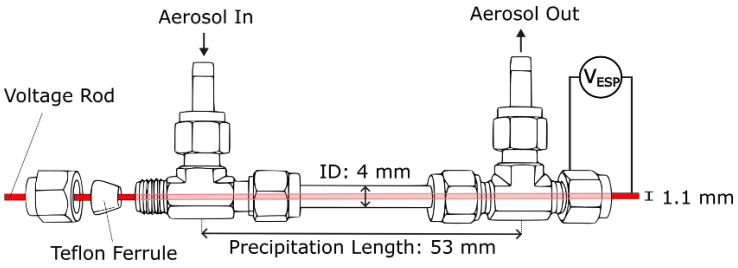

Figure S-3. Schematic of the electrostatic precipitator. ID: inner diameter

The transmission through the ESP was measured for each particle size up to 20 nm by passing monodisperse particles classified by the Vienna-type DMA through the ESP (see Figure S-4). Applying a voltage of 2 kV was sufficient to remove all sub-20 nm particles, and 10 V removed all ions.

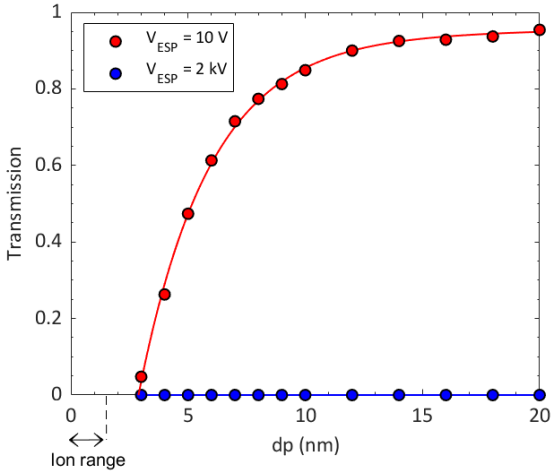

Figure S-4. Transmission of the ESP at the ion precipitating (V_{ESP} = 10 V) and particle precipitating setting (V_{ESP} = 2 kV). The transmission was calculated with respect to the setting V_{ESP} = 0 V.

Section S-5. Calibration factor for charge fraction measurement

Figure S-5 shows the calibration factor C used in Eq. 15 in the main text, that accounts for particle losses due to operating the ESP at 10 V. Setting the ESP at 10 V during the I_{FCE} measurement is necessary, as it ensures that ions produced by the candidate charge conditioner are fully precipitated, thereby preventing interference with the FCE signal as they travel downstream.

This factor was determined from a separate set of measurements conducted without the charge conditioner installed downstream DMA-1. Particles entering the measuring stage are therefore either positively or negatively charged as they are classified by the Vienna-type DMA, and $f_{\pm 1}$ is therefore known ($f_{\pm 1} = 1$ or 0, depending on DMA-1 polarity). This enables C to be determined from Eq. 15.

Given the parallel CPC and FCE configuration, the correction factor C accounts not only for particle losses in the FCE but also for the detection efficiency of the CPC.

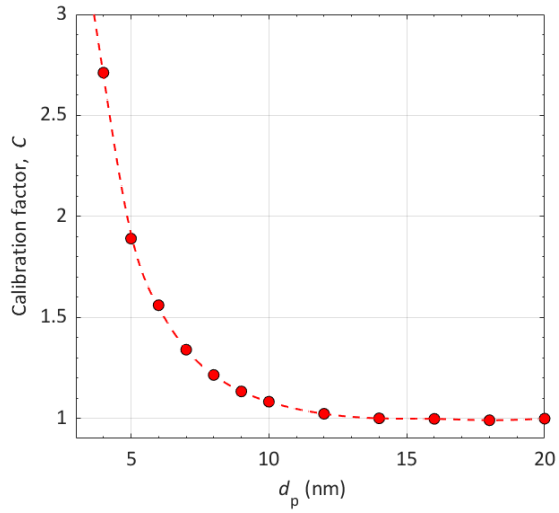

Figure S-5. Calibration factor C for each particle size. This factor was determined by using the calibration setup.

Section S-6. Transmission of half-mini DMA

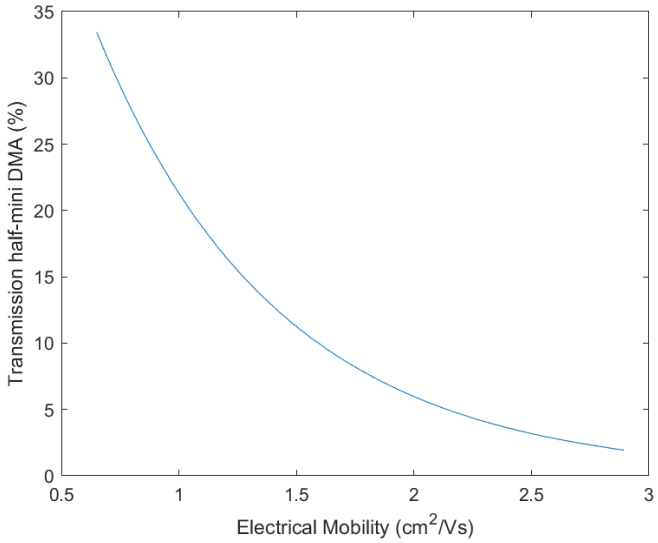

Figure S-6. Transmission through the half-mini DMA for ions of different electrical mobility, at a sheath flow and aerosol flow rate of 300 and 3 lpm, respectively (Cai et al., 2018). The electrical mobility distributions were corrected according to the ion transmission.

Section S-7. Shifting mean ion mobility downstream the charge conditioner

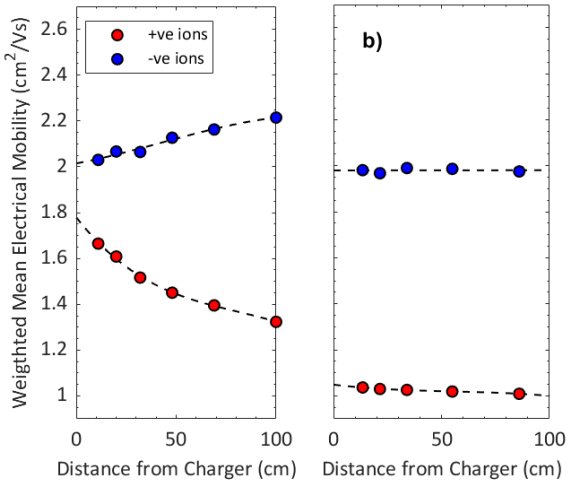

Figure S-7. Weighted mean ion electrical mobility as a function of distance between ion formation in the charge conditioner and their classification in DMA-2, shown for configurations without (a) and with (b) a 1-cm piece of silicone conductive tubing installed upstream of the charge conditioner. This measurement was performed using ions created in 5.0 nitrogen with a flow rate of 5 lpm. No aerosol particles are involved in this measurement.

Figure S-7. Weighted mean ion electrical mobility as a function of distance between ion formation in the charge conditioner and their classification in DMA-2, shown for configurations without (a) and with (b) a 1-cm piece of silicone conductive tubing installed upstream of the charge conditioner. This measurement was performed using ions created in 5.0 nitrogen with a flow rate of 5 lpm. No aerosol particles are involved in this measurement. shows the weighted mean ion electrical mobility as a function of the distance between the charge conditioner and DMA. For this measurement particle-free nitrogen was used. It shows a significant shift in the weighted mean electrical mobility as a function of the distance between the charge conditioner and the DMA when silicone conductive tubing is omitted. In contrast, this shift is significantly reduced when silicone conductive tubing is employed.

Ions are mobility-classified by the half-mini DMA located some distance downstream of the charge conditioner. One possible explanation for the observed shift is differential wall losses, whereby high-mobility ions are preferentially lost to the tubing walls during transport. This effect is expected to be most pronounced for broad mobility distributions, as the case when silicone conductive tubing is omitted (see Fig. 2). The much smaller shift observed when silicone conductive tubing is used supports this hypothesis, as the mobility distribution is in this case considerably narrower (see Fig. 2), making the weighted mean mobility less sensitive to wall losses.

A further explanation is that charge transfer reactions continue to occur downstream of the charge conditioner because the charge distribution among the ion population has not yet reached equilibrium. Positive charges are preferentially transferred to species with the highest proton affinity, whereas negative charges are transferred to the most electronegative species. If different species have similar affinities for the charge, redistribution may proceed more slowly, allowing the mobility distribution to continue evolving during transport. When silicone conductive tubing is employed, however, the ion population is dominated by VMS ions, which have a high proton affinity and therefore strongly retain

the positive charge. In this case, further charge redistribution is therefore minimal, resulting in little or no shift in the weighted mean electrical mobility during transport.

Section S-8. The effect of relative humidity on the charger ion mobility distribution

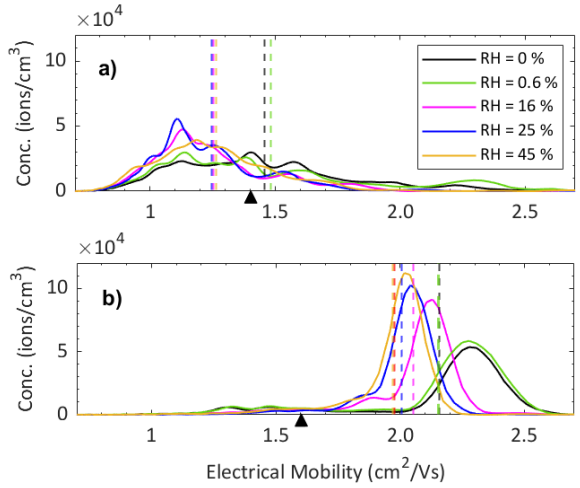

Figure S-8. Charger ion properties of positive (a) and negative (b) ions produced at different relative humidities ranging from 0% to 45%. The vertical striped lines indicate the weighted mean of the distribution of the respective color, and the triangles show the mobility values used in the Wiedensohler (1988) approximation.

Section S-9. Hoppel & Frick vs. Wiedensohler with same ion properties

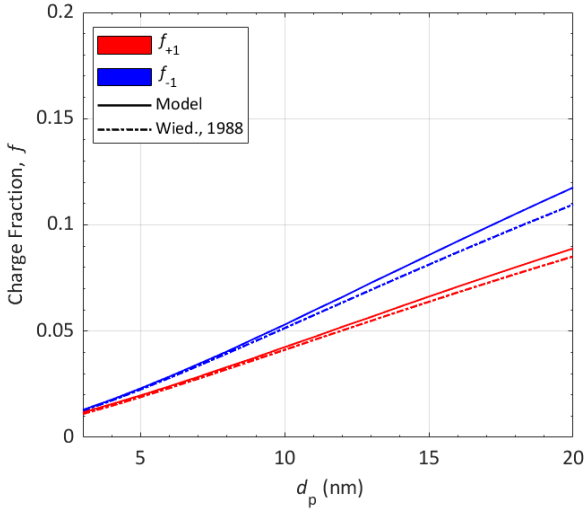

Figure S-9. Charge fractions determined by the Wiedensohler (1988) approximation and the Hoppel & Frick-based model when the ion properties assumed in the approximation are used in the model (i.e., Z+=1.35 $cm^2V^{-1}s^{-1}$, Z-=1.60 $cm^2V^{-1}s^{-1}$, m+=140 and m-=101 Da). It shows that there is a relatively good agreement, which is because the approximation is based on the Hoppel & Frick-based model.

Section S-10. Effect on charge fractions when using silicone tubing

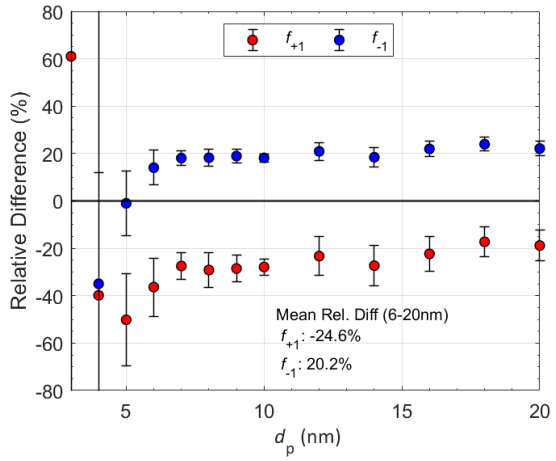

Figure 1. Relative difference in particle charge fraction between the cases when the conductive silicone tubing was used or not in the experiments.

Section S-11. Relation between charge fractions and ion properties

As shown by Chen & Jiang (2018), the ratio of charge fractions f_{+q}/f_{-q} for particles in the continuum regime of charge q can be approximated by an expression derived from Gunn & Woessner (1956), which is

$$f_{+q}/f_{-q} = (Z_i^+/Z_i^-)^{2q} \qquad \text{Eq. S-2}$$

Although sub-20 nm particles are not in the continuum size regime, we can still test this relationship in that size regime by comparing the calculated f_{+q}/f_{-q} to that determined using the well-established Hoppel & Frick theory, which includes detailed calculations involving modelling the interactions between ions and particles. Herein, we assume that q=1, as particles in this size range carry at most one charge (Wiedensohler, 1988). Furthermore, random values of Z_i^+ and Z_i^- were used as model input within a realistic mobility range of 0.8 - 2.5 cm^2/Vs, together with the corresponding c_i^+ and c_i^-, with the constraint $Z_i^+ < Z_i^-$,

Figure S-10 shows how f_{+1}/f_{-1} determined by Eq. S-2 compares with that determined by the model based on Hoppel-Frick theory. It shows that even for sizes close to the free molecular regime (i.e., 20 nm particles) there is a relatively good agreement (R^2 = 0.99), however with a scatter (RSME=0.088 for 20-nm particles) that increases as particle sizes decreases.

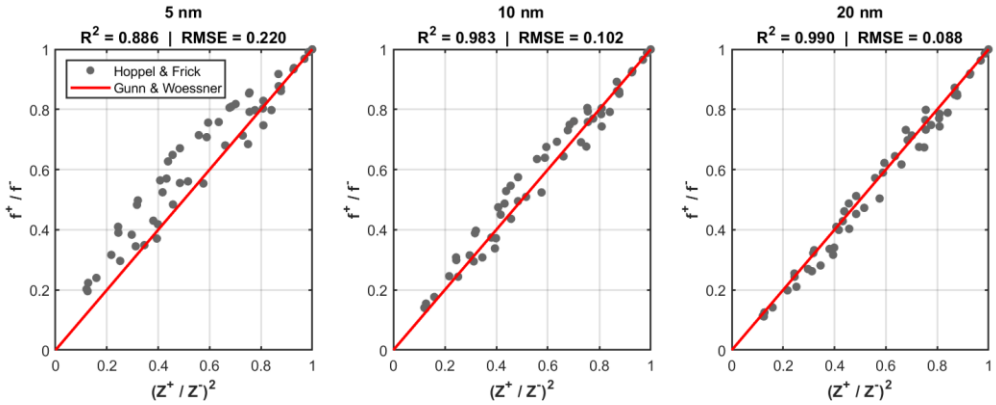

Figure S-10. f_+/f_- against $(Z_i^+/Z_i^-)^2$ for d_p = 5, 10 and 20 nm, following the relation derived from Gunn & Woessner (Eq. S-2). The f_{+1}/f_{-1} determined from the model based on Hoppel & Frick theory was calculated by generating random combinations of Z_i^+ and Z_i^-, with values chosen in a realistic range between 0.8 and 2.5 cm^2/Vs, and $Z_i^+ < Z_i^-$.

The scatter stems from the fact that the charge fraction ratio f_{+1}/f_{-1} is not solely a function of the mobility ratio Z_i^+/Z_i^-, but a complex function of various other variables, including ion mass, ion thermal speed, mean free path, that are non-linearly related to the combination coefficient that determines the charge fractions (see Eq. 5 in the main text). Consequently, f_{+1}/f_{-1} cannot be accurately expressed as a function of Z_i^+/Z_i^- alone.

In the free molecular regime, ion attachment is governed primarily by ion-particle collision kinetics (governed by c_i, as shown in Eq. S-1), whereas charging in the continuum regime is increasingly influenced by diffusive transport (governed by D_i, relating linearly to Z_i). Since the sub-20 nm regime approaches the free molecular regime, the relation in Eq. S-2 can be improved by expressing the ion properties by c_i^+ and c_i^-. As shown in Figure S-11, the relationship

$$f_{+1}/f_{-1} = (c_i^+/c_i^-)^{\alpha(d_p)} \qquad \text{Eq. S-3}$$

where $\alpha(d_p)$ is obtained from a linear regression fit for each particle diameter d_p, provides a significantly more accurate approximation of f_+/f_-. Especially for 20 nm particles this correlation is excellent, with an R^2 of 1.000 and a low scatter (RSME = 0.011).

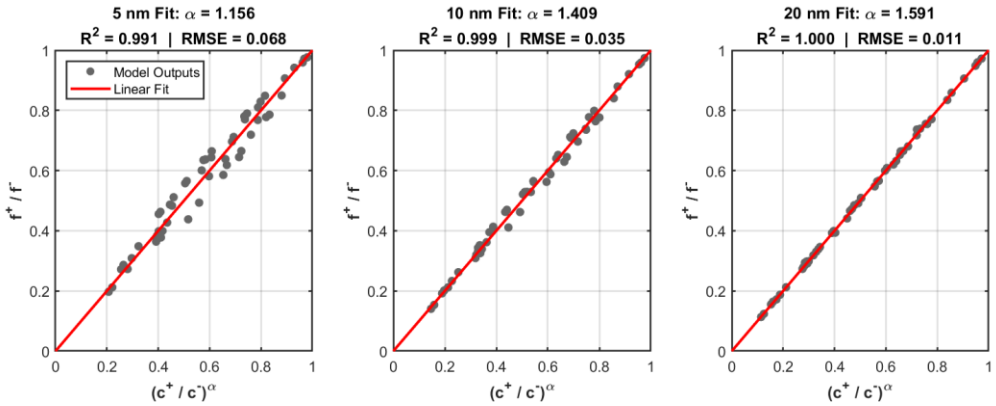

Figure S-11. $(c_+/c_-)^\alpha$ plotted against f_{+1}/f_{-1} for different d_p. The exponent α was found through linear regression analysis for each d_p.

The very low scatter at a size of 20 nm (Figure S-11c) is striking, because it indicates that, f_{+1}/f_{-1} primarily depends on c_i^+/c_i^- for 20 nm particles. Interestingly, the relation worsens again for smaller

d_p, indicating that other variables in Eq. 5 that non-linearly relate to $c_\mathrm{i}^+/c_\mathrm{i}^-$ become dominant, such as the electrostatic potential ϕ.

The particularly strong agreement observed at 20 nm can be exploited to estimate ion properties using Eq. S-3. Since, by definition, $f_{+1}/f_{-1} = N_{+1}/N_{-1}$, where N is the particle concentration in a given charge state, the charge fraction ratio can be determined directly from measurements using MPSS. Consequently, the ion concentration ratio $c_\mathrm{i}^+/c_\mathrm{i}^-$ can be approximated from measurements of N_{+1}/N_{-1} for 20 nm particles.

Explanation of the above observations from theory

For sub-20 nm particles, we assume that multiply charged particles are negligible (Wiedensohler, 1988). The birth-and-death equations therefore simplify to

$$\frac{dN_{+1}}{dt} = n^+\beta_0^+N_0 - n^-\beta_{+1}^-N_{+1} \qquad \text{Eq. S-4}$$

$$\frac{dN_{-1}}{dt} = n^-\beta_0^-N_0 - n^+\beta_{-1}^+N_{-1} \qquad \text{Eq. S-5}$$

In the steady-state, dN_{+1}/dt and dN_{-1}/dt are equal to zero. Assuming equal concentrations of positive and negative ions within the charge conditioner, Eq. S-4 and Eq. S-5 can be rearranged to (Adachi et al., 1985):

$$\frac{N_{+1}}{N_{-1}} = \frac{\beta_0^+\beta_{-1}^+}{\beta_0^-\beta_{+1}^-} \qquad \text{Eq. S-6}$$

Eq. S-6 is valid across all size regimes. In the free molecular regime, the combination coefficients, β_{-1}^+ and β_{+1}^- (ions combining with particles of opposite charge state), are approximately equal. Therefore, in the free molecular regime Eq. S-6 can be approximated by

$$\frac{N_{+1}}{N_{-1}} = \frac{\beta_0^+}{\beta_0^-} \qquad \text{Eq. S-7}$$

At the free molecular limit

$$\beta \propto {d_p}^2 c \cdot E.F. \qquad \text{Eq. S-8}$$

where E.F is the enhancement factor that depends on both the Coulomb and image forces between particle and ion. Combining Eq. S-7 and Eq. S-8 yields

$$\frac{N_{+1}}{N_{-1}} = \frac{{d_p}^2 c_\mathrm{i}^+ \, (E.F.)_0^+}{{d_p}^2 c_\mathrm{i}^- (E.F.)_0^-} \qquad \text{Eq. S-9}$$

For a neutral particle, Coulomb enhancement is zero, while the image force enhancement is assumed to be identical for positive and negative ion polarities, i.e., $(E.F.)_0^+/(E.F.)_0^- = 1$, which yields

$$\frac{N_{+1}}{N_{-1}} = \frac{c_\mathrm{i}^+}{c_\mathrm{i}^-} \qquad \text{Eq. S-10}$$

where N_{+1}/N_{-1} is by definition equal to f_{+1}/f_{-1}. We therefore now have two distinct limits, where on one hand

$$\frac{f_{+1}}{f_{-1}} = \frac{c_{\mathrm{i}}^{+}}{c_{\mathrm{i}}^{-}} \qquad \text{Eq. S-11}$$

is valid in the free molecular regime and on the other hand,

$$\frac{f_{+1}}{f_{-1}} = \left(\frac{Z_{\mathrm{i}}^{+}}{Z_{\mathrm{i}}^{-}}\right)^{2} \qquad \text{Eq. S-12}$$

for the continuum regime (Chen & Jiang, 2018).

As can be shown using Kilpatrick and gas kinetic theory, that the Z-ratio can be expressed in terms of the c-ratio, i.e.,

$$\frac{Z_{\mathrm{i}}^{+}}{Z_{\mathrm{i}}^{-}} \approx \left(\frac{c_{\mathrm{i}}^{+}}{c_{\mathrm{i}}^{-}}\right)^{0.755} \qquad \text{Eq. S-13}$$

This shows that for singly charged particles f_{+1}/f_{-1} can be approximated in terms of $(c_{\mathrm{i}}^{+}/c_{\mathrm{i}}^{-})^{\alpha}$. The exponent α reflects the relative contributions of continuum and free-molecular charging mechanisms and therefore depends on particle size. As Figure S-11 shows, this approximation has highest precision and accuracy for 20 nm particles.

References

Adachi, M., Kousaka, Y., & Okuyama, K. (1985). Unipolar and bipolar diffusion charging of ultrafine aerosol particles. *Journal of Aerosol Science*, *16*(2), 109–123. https://doi.org/10.1016/0021-8502(85)90079-5

Cai, R., Attoui ,Michel, Jiang ,Jingkun, Korhonen ,Frans, Hao ,Jiming, Petäjä ,Tuukka, & and Kangasluoma, J. (2018). Characterization of a high-resolution supercritical differential mobility analyzer at reduced flow rates. *Aerosol Science and Technology*, *52*(11), 1332–1343. https://doi.org/10.1080/02786826.2018.1520964

Chen, X., & Jiang, J. (2018). Retrieving the ion mobility ratio and aerosol charge fractions for a neutralizer in real-world applications. *Aerosol Science and Technology*, *52*(10), 1145–1155. https://doi.org/10.1080/02786826.2018.1498587

Gunn, R., & Woessner, R. H. (1956). *MEASUREMENTS OF THE. SYSTEMATIC ELECTRIFICATION -:OF AEROSOLS*.

Keller, B. O., Sui, J., Young, A. B., & Whittal, R. M. (2008). Interferences and contaminants encountered in modern mass spectrometry. *Analytica Chimica Acta*, *627*(1), 71–81. https://doi.org/10.1016/j.aca.2008.04.043

Kilpatrick, W. D. (1971). An experimental mass-mobility relation for ions in air at atmospheric pressure. *Proc. Annu. Conf. Massspectrosc*, *19*, 320–325.

Mäkelä, J. M., Jokinen, V., Mattila, T., Ukkonen, A., & Keskinen, J. (1996). Mobility distribution of acetone cluster ions. *Journal of Aerosol Science*, *27*(2), 175–190. https://doi.org/10.1016/0021-8502(95)00560-9

White, H. J. (1951). Particle Charging in Electrostatic Precipitation. *Transactions of the American Institute of Electrical Engineers*, *70*(2), 1186–1191. https://doi.org/10.1109/T-AIEE.1951.5060545

Wiedensohler, A. (1988). An approximation of the bipolar charge distribution for particles in the submicron size range. *Journal of Aerosol Science*, *19*(3), 387–389. https://doi.org/10.1016/0021-8502(88)90278-9